Microstructure and Magnetic Properties of $Ni_2(Mn,Fe)Ga$ Heusler Alloys Rapidly Solidified by Melt Spinning

R.V.S. PRASAD, M. SRINIVAS, M. MANIVEL RAJA, and G. PHANIKUMAR

The microstructure and magnetic properties of Ni_2MnGa base alloys with ''Fe'' substitution in place of ''Mn'' are studied. The processing technique used is melt spinning at wheel speeds of 20 m/s and 30 m/s followed by annealing at 1273 K (1000 °C) for 1 hour. Fe content is varied from 2 at. pct to 11 at. pct for alloys of $Ni_{50}Mn_{(25-x)}Fe_xGa_{25}$ with Heusler stoichiometry. Austenite with B2 partial atomic ordering and premartensitic tweed structures were found at room temperature for all the alloys at different wheel speeds. After annealing at 1273 K (1000 °C) for 1 hour, austenite phase with $L2_1$ Heusler atomic ordering is stabilized in samples of all the processing conditions. Saturation magnetization, martensitic transformation temperature, and Curie temperature are measured. Martensite temperature and Curie temperature increase in proportion to iron content in the alloy. Saturation magnetization is sensitive to the phase content and compositional inhomogeneities.

DOI: 10.1007/s11661-013-2124-x

I. INTRODUCTION

THE research on Ni_2MnGa-based ferromagnetic shape memory alloys has been intense during the last decade owing to their application as a potential material in the field of sensors and actuators.[1,2] The microstructure, shape memory effect, magnetic properties, cycling characteristics, and ultrasound-induced martensitic transitions of Ni-Mn-Ga alloys have been studied.[3–5] However, it is difficult to manufacture these alloys in the form of thin plates or wires due to their limited ductility. The relatively high vapor pressure of manganese over its melt leads to composition variation during liquid metal processing of these alloys. Substituting Mn with Fe is of interest for commercialization. Earlier researchers explored the addition of different alloying additions to enhance the toughness of Ni_2MnGa alloy while attempting to retain its magnetic and thermoelastic properties.[6,7]

Although the effect of different elements has been studied in the Ni-Mn-Ga system, the open literature on the phase content and magnetic properties of rapidly solidified Ni-Mn-Ga alloys is limited.[8,9] Earlier studies on melt-spun Ni_2MnGa alloys revealed the formation of martensite, nanocrystalline, and amorphous phases.[10,11] Ribbons of Ni_2MnGa melt spun at high wheel speeds resulted in amorphous and nanocrystalline phases, and exhibited poor magnetic properties. The current study is based on the premise that possibilities offered by rapid solidification such as extended solid solubility and metastable microstructure formation could lead to interesting magnetic properties. In this study, substitution of iron in place of manganese is attempted to study its effect on structure and magnetic properties. The concentration of iron is varied (2, 5, 8, and 11 at. pct) while keeping the nominal composition close to Heusler composition.

II. EXPERIMENTAL METHODS

A series of four alloys with compositions of $Ni_{50}Mn_{(25-x)}Fe_xGa_{25}$ ($x = 2, 5, 8, 11$ at. pct) is prepared by arc melting of 99.99 pct pure nickel, manganese, iron, and gallium in argon atmosphere. Compositions will be referred to by their iron content for brevity. All composition values are given in at. pct, and the nominal and actual values detected by scanning electron microscope for energy dispersive analysis of X-rays (SEM-EDX) are listed in the Table I along with corresponding e/a ratio values. Five-gram button samples are prepared and melted four times to ensure a highly homogeneous ingot. A conventional rotating copper wheel is used to obtain melt-spun ribbons in a vacuum chamber flushed with argon and held at a pressure of 10^{-5} m bar. Two different wheel speeds of 20 m/s and 30 m/s are chosen for each alloy composition after several trials to achieve a good quality of ribbon with uniform thickness in the range of 30 to 35 μm and 20 to 25 μm, respectively. These wheel speeds correspond to the two extreme velocities of the wheel that ensure a continuous and smooth ribbon. The speeds will be referred to concisely as low (20 m/s) and high (30 m/s). For each of the four compositions, approximately 5 g of alloy is induction melted in a quartz tube with an orifice diameter of 0.8 mm and then

R.V.S. PRASAD, formerly Research Scholar with the Department of Metallurgical and Materials Engineering, Indian Institute of Technology Madras, Chennai- 600036, India, is now Visiting Scientist with the Korea Institute of Materials Science, Changwondaero, Seongsan-gu, Changwon, Gyeongnam 642-831, South Korea. M. SRINIVAS, Scientist C, and M. MANIVEL RAJA, Scientist F, are with the Advanced Magnetic Materials Group, Defence Metallurgical Research Laboratory, Hyderabad 500058, India. G. PHANIKUMAR, Associate Professor, is with the Department of Metallurgical and Materials Engineering, Indian Institute of Technology Madras. Contact e-mail: gphani@iitm.ac.in

Manuscript submitted January 31, 2011.
Article published online November 23, 2013

Table I. Nominal and Actual Stoichiometry by SEM-EDX Analysis of the Arc-Melted Samples with Corresponding *e/a* Ratios

S. No.	Condition	Aimed (*e/a* Ratio)	Actual (*e/a* Ratio)	Alloy Composition (Aimed)	SEM-EDX Analysis (Actual Composition in at. pct) Ni	Mn	Fe	Ga
1	as cast	7.52	7.57	$Ni_{50}Mn_{23}Fe_2Ga_{25}$	55.0	15.0	2.5	27.5
2	as cast	7.55	7.60	$Ni_{50}Mn_{20}Fe_5Ga_{25}$	54.0	13.0	6.0	27.0
3	as cast	7.58	7.73	$Ni_{50}Mn_{17}Fe_8Ga_{25}$	55.0	11.5	8.5	25.0
4	as cast	7.61	7.76	$Ni_{50}Mn_{14}Fe_{11}Ga_{25}$	55.0	9.0	11.0	25.0

ejected with a 1.10-bar back pressure of argon gas. The ribbons are then vacuum sealed in a quartz tube and annealed at 1273 K (1000 °C) for 1 hour. The samples of all conditions are thinned down using an ion mill for characterization using a 200-keV transmission electron microscope (TEM). Phase identification of melt-spun ribbon samples has been performed using X-ray diffraction (XRD) studies with Cu-Kα radiation. Room-temperature magnetic and thermomagnetic measurements on melt-spun ribbon samples are obtained by a vibrating sample magnetometer (VSM) and susceptibility meter.

III. EXPERIMENTAL RESULTS

A. *Microstructure and Phase Analysis*

The XRD patterns of melt-spun ribbon samples of $Ni_{50}Mn_{(25-x)}Fe_xGa_{25}$ alloy at both the wheel speeds showed peaks of the austenite phase with B2 ordering. Also, the peaks are sharp, indicating polycrystalline nature of the sample and absence of amorphous content. Figures 1(a) and (b) show XRD patterns of 2, 5, 8, and 11 at. pct Fe alloy melt-spun ribbons at 20 m/s and 30 m/s wheel speeds. Similarly, Figures 1(c) and (d) show XRD patterns of 2, 5, 8, and 11 at. pct Fe alloy melt-spun ribbons at 20 m/s and 30 m/s wheel speeds after annealing. The XRD patterns of the samples melt spun at wheel speeds of 20 m/s and 30 m/s (shown in Figures 1(a) and (b)) indicate that the samples contain predominantly single-phase microstructure and are indexed to austenite phase with B2 partial atomic ordering. However, after annealing at 1273 K (1000 °C) for 1 hour, the corresponding melt-spun ribbon samples completely transform to fully ordered $L2_1$ structure as indexed in Figures 1(c) and (d).

Microscopy results are detailed first for samples melt spun at low speed. Figure 2 shows transmission electron microscopy of a 5 at. pct-Fe alloy sample. The selected-area electron diffraction (SAED) pattern taken along the [0$\bar{4}$4] zone axis and indexed to B2 ordering confirms the austenite phase of Ni_2(Mn,Fe)Ga alloy. The austenite grains, as seen in the bright-field image, are fairly equiaxed with an average grain size between 0.5 and 1.5 μm.

A bright-field image of 8 at. pct-Fe alloy ribbon and the corresponding SAED pattern taken along [$\bar{4}$40] zone axis are shown in Figures 3(a) and (b), respectively. In this sample, there are regions exhibiting two different contrasts of grains (Figure 3(c)). A bright-field image at higher magnification (Figure 3(d)) indicates that these regions could be of premartensitic tweed structure. This contrast is very similar to several earlier observations on tweed structures available in the open literature in several systems such as Cu-Be, Ni-Al, and $Nd_{(1-x)}$-Sr_xMnO_3.[12–17] Kartha *et al.*[18,19] have analyzed these contrasts as due to pretransitional tweed patterns driven by disorder.

Scanning probe microscopy of the 8 at. pct-Fe alloy ribbons melt spun at low speed is shown in Figure 4. Atomic force microscopy (AFM) in contact mode shows (Figure 4(a)) the grains to be equiaxed and about 1 to 2 μm. Magnetic force microscopy (MFM) shows (Figure 4(b)) the magnetic domains in this alloy to be around the same size as the grains.

In the TEM bright-field image of the 11 at. pct-Fe alloy sample shown in Figure 5(a), one can observe the tweed structure due to magnetic tweed contrast. Such structures are limited to small regions with an occasional presence in the Fe-11 at. pct sample alone before heat treatment. Figure 5(b) shows a bright-field image of 11 at. pct-Fe alloy sample revealing that the alternate twins of martensite phase evolve from triple junctions. The SAED pattern confirms martensite phase with nonmodulated tetragonal crystal structure (as shown in Figure 5(c)) and the zone axis of the pattern is along [044].

The samples melt spun at lower speeds have shown the presence of tweed contrasted regions only for alloys containing 8 at. pct-Fe and 11 at. pct-Fe. However, the samples melt spun at higher speeds have shown a different phase evolution as indicated below.

Figures 6(a) and (b) show the TEM bright-field images and SAED pattern of the 5 at. pct-Fe alloy sample melt spun at a higher wheel speed. The SAED pattern taken with [04$\bar{4}$] zone axis is indexed to B2 ordering and belongs to austenite phase of Ni_2(Mn,Fe)-Ga alloy. Figure 6(c) shows the typical tweed contrast region. Similarly, the TEM studies performed on an 8 at. pct-Fe alloy sample (Figure 7) and 11 at. pct-Fe alloy sample (Figure 8) show that the major phase is of B2 structure, and a mixture with tweed contrast co-exists in the microstructure. These studies show that premartensitic tweed structure is observed in all the samples melt spun at a high wheel speed.

The annealed samples of all the processing conditions are characterized by X-ray diffraction, and corresponding peaks have been indexed to $L2_1$ Heusler atomic ordering (Figures 1(c) and (d)). Super lattice reflections are observed as compared to the melt-spun 20 m/s wheel speed sample, which are characteristic of

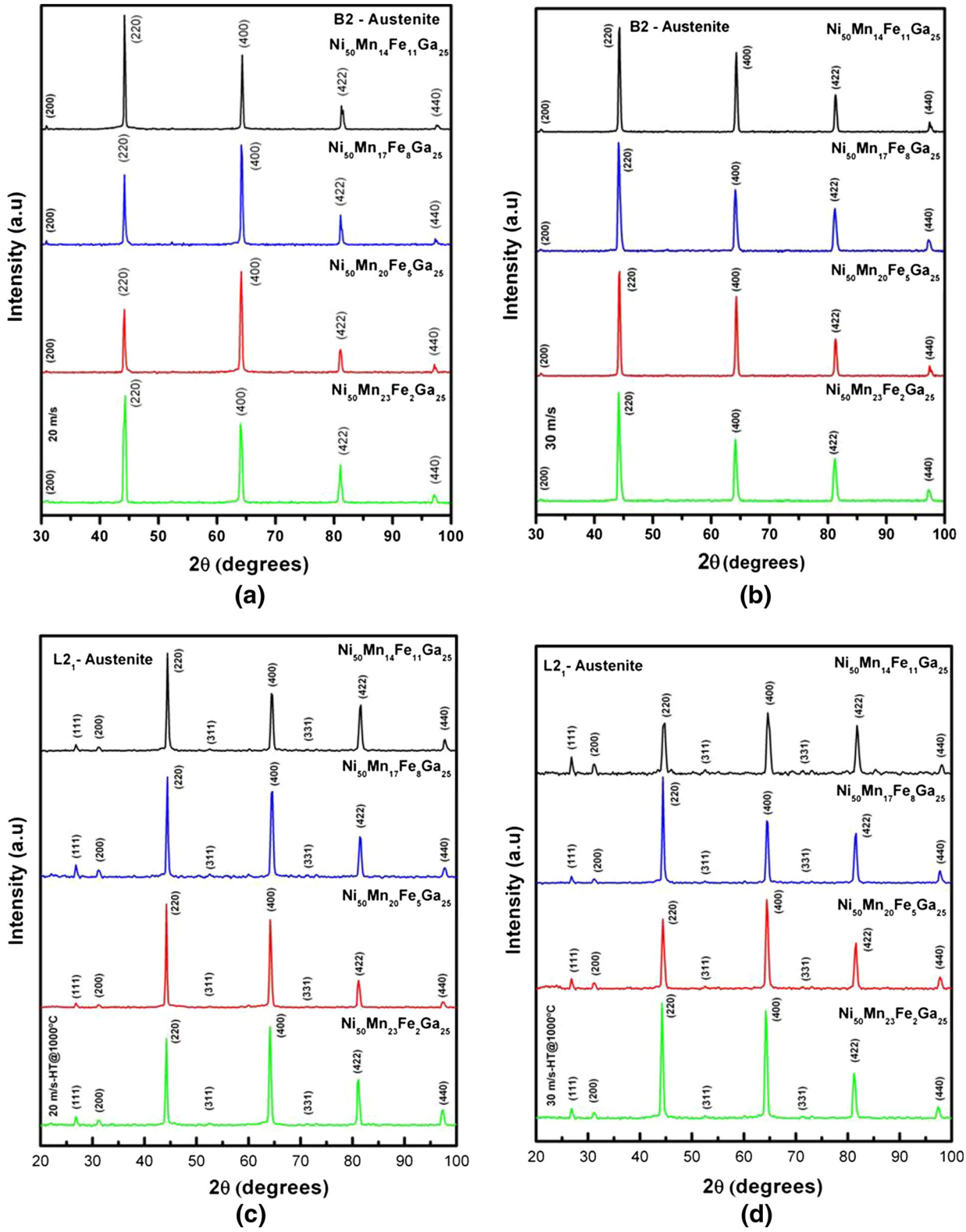

Fig. 1—XRD patterns of $Ni_{50}Mn_{(25-x)}Fe_xGa_{25}$ alloy melt-spun samples: (*a*) 20 m/s wheel speed, (*b*) 30 m/s wheel speed, (*c*) 20 m/s wheel speed after annealing, and (*d*) 30 m/s wheel speed after annealing.

$L2_1$ ordering. Similarly, after annealing at 1273 K (1000 °C) for 1 hour, all the ribbons of different "Fe" concentrations (2, 5, 8, and 11 at. pct) and melt-spun at higher wheel speed (30 m/s) show that the X-ray diffraction peaks confirm to austenite phase with $L2_1$ atomic ordering.

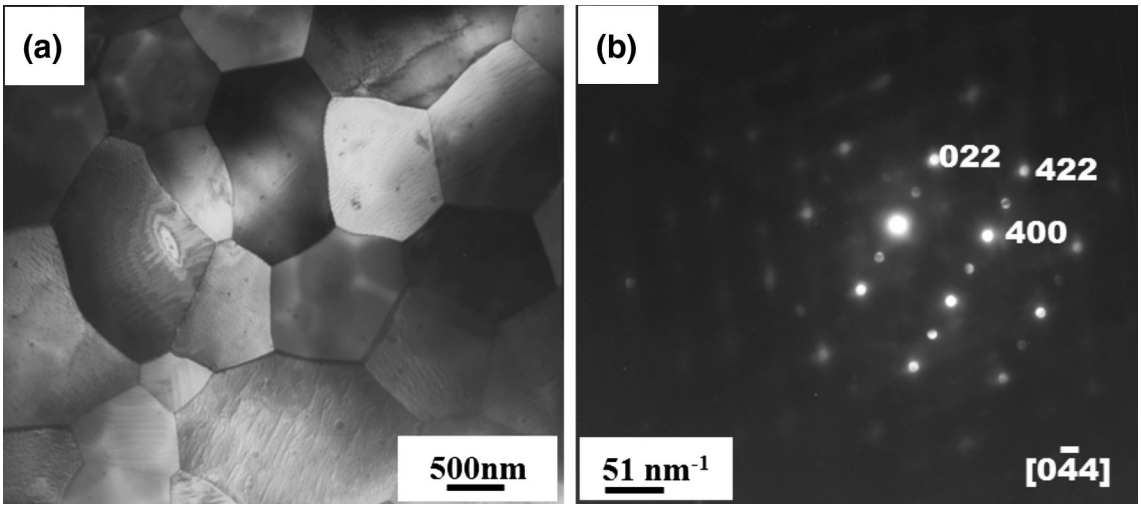

Fig. 2—Transmission electron microscopy of $Ni_{50}Mn_{20}$ Fe_5Ga_{25} ribbon melt spun at a wheel speed of 20 m/s: (*a*) bright-field image and (*b*) corresponding SAED pattern taken along [0$\bar{4}$4] zone axis indexed to B2 structure.

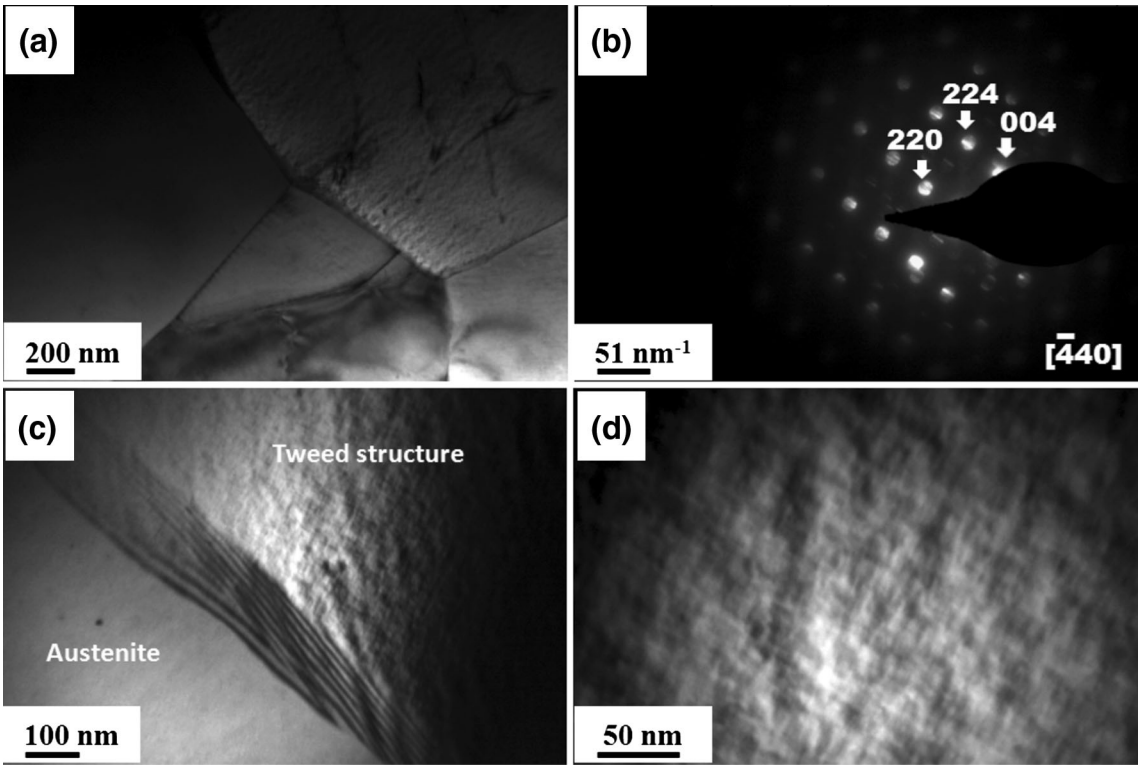

Fig. 3—Transmission electron microscopy of $Ni_{50}Mn_{17}$ Fe_8 Ga_{25} alloy melt spun at low wheel speed: (*a*) bright-field image showing austenite phase, (*b*) corresponding SAED pattern taken along [$\bar{4}$40] zone axis, (*c*) bright-field image shows existence of both austenite and tweed structure, and (*d*) bright-field image of tweed structure at a higher magnification.

B. *Magnetic and Structural Properties*

Magnetic and structural properties such as saturation magnetization (*M*s), martensitic transformation temperature (T_m) and Curie temperature (T_C) are measured by using different magnetic characterization tools like a vibrating sample magnetometer and susceptibility meter.

The results on saturation magnetization for 20 m/s wheel speed before and after annealing on Ni_2(Mn,Fe)-Ga Heusler alloy for different ''Fe'' concentrations with magnetization *vs* magnetic field plots are shown in Figures 9(a) and (b), respectively. Similarly, magnetization *vs* temperature plots for 20 m/s wheel speed for all the ''Fe'' concentrations are shown in Figure 9(c) by depicting the average martensite transformation temperature and Curie temperatures marked with square hatched and open boxes, respectively. The room-temperature magnetic and thermomagnetic measurements are not detailed for other conditions here for brevity.

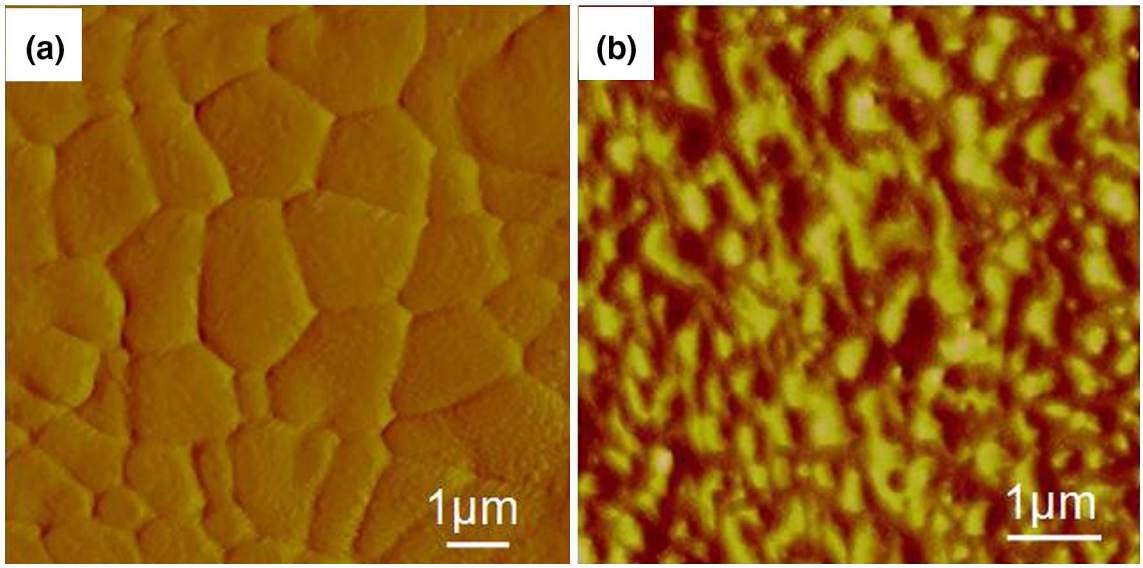

Fig. 4—(*a*) AFM contact mode image of $Ni_{50}Mn_{20}$ Fe_8Ga_{25} alloy melt spun at wheel speed of 20 m/s. (*b*) MFM image of same sample.

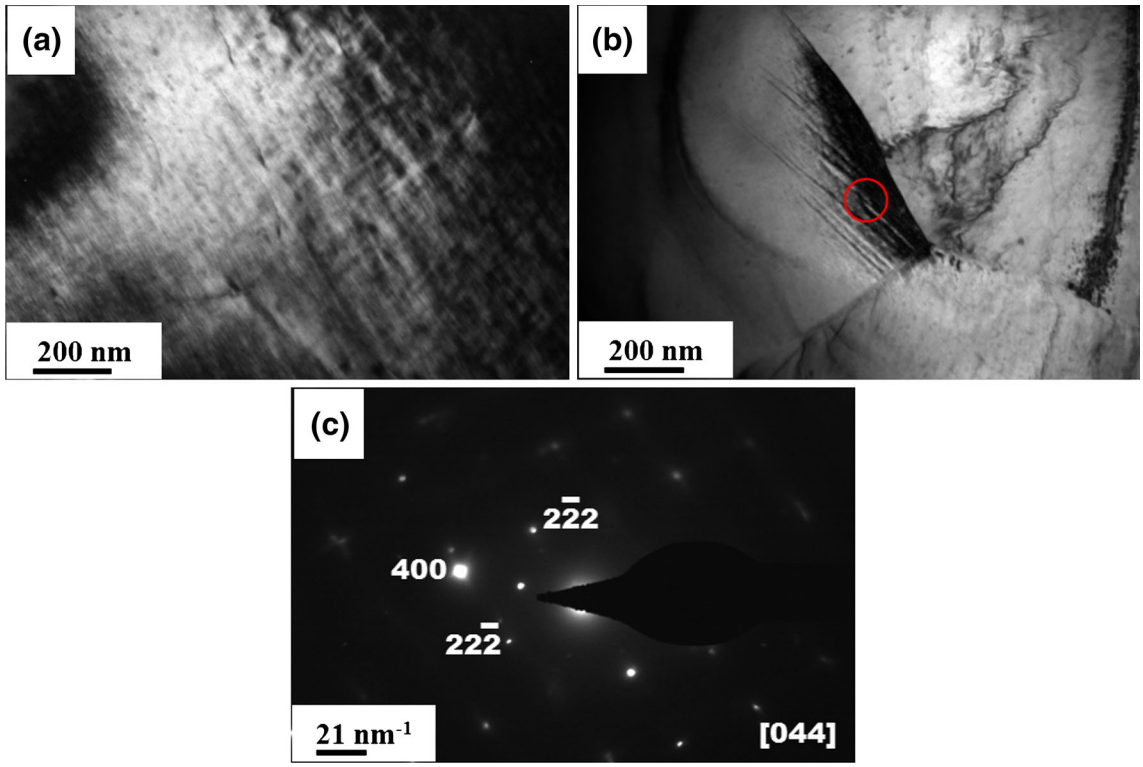

Fig. 5—Transmission electron microscopy of $Ni_{50}Mn_{14}Fe_{11}Ga_{25}$ alloy melt spun at low wheel speed: (*a*) bright-field image showing tweed structure, (*b*) bright-field image showing martensite region at triple junction, and (*c*) corresponding SAED pattern taken from martensite phase (marked in red circle) indexed to nonmodulated tetragonal structure along [044] zone axis.

However, properties such as saturation magnetization, martensite transformation temperature, and Curie temperature were shown in Figure 10 as a function of average iron content or *e*/*a* ratio.

Saturation magnetization values of all samples are plotted as function of nominal average iron content of the alloy as well as the corresponding *e*/*a* ratio (Figure 10(a)). Saturation magnetization values are more or less similar with the Fe content from 2 at. pct up to 11 at. pct for 20 m/s and 30 m/s melt-spun ribbon samples with marginal differences. However, after annealing, the saturation magnetization values are decreasing for 20 m/s and 30 m/s melt-spun samples for all the Fe concentrations or *e*/*a* ratio values. These observations are in good agreement with existing literature as indicated in the study by Jin *et al.*[20]

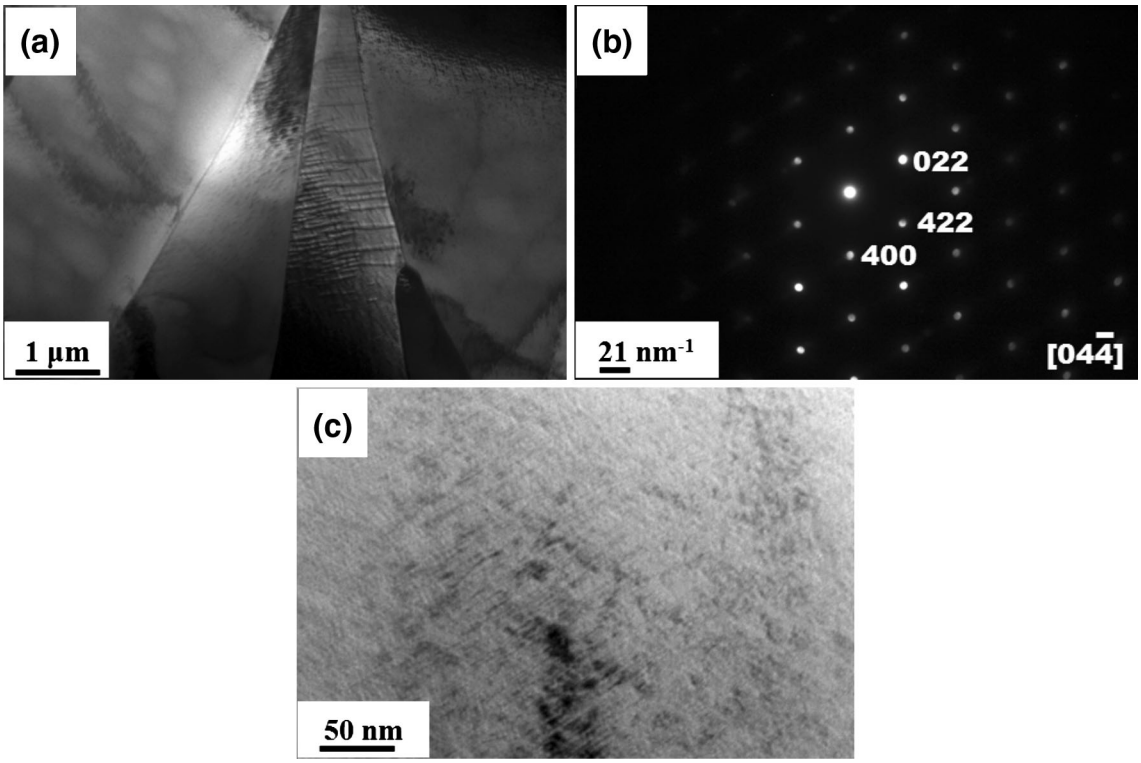

Fig. 6—Transmission electron microscopy of $Ni_{50}Mn_{20}Fe_5Ga_{25}$ alloy melt spun at high wheel speed: (*a*) bright-field image showing austenite phase, (*b*) corresponding SAED pattern taken along [044̄] zone axis, and (*c*) bright-field image showing tweed structure at higher magnification.

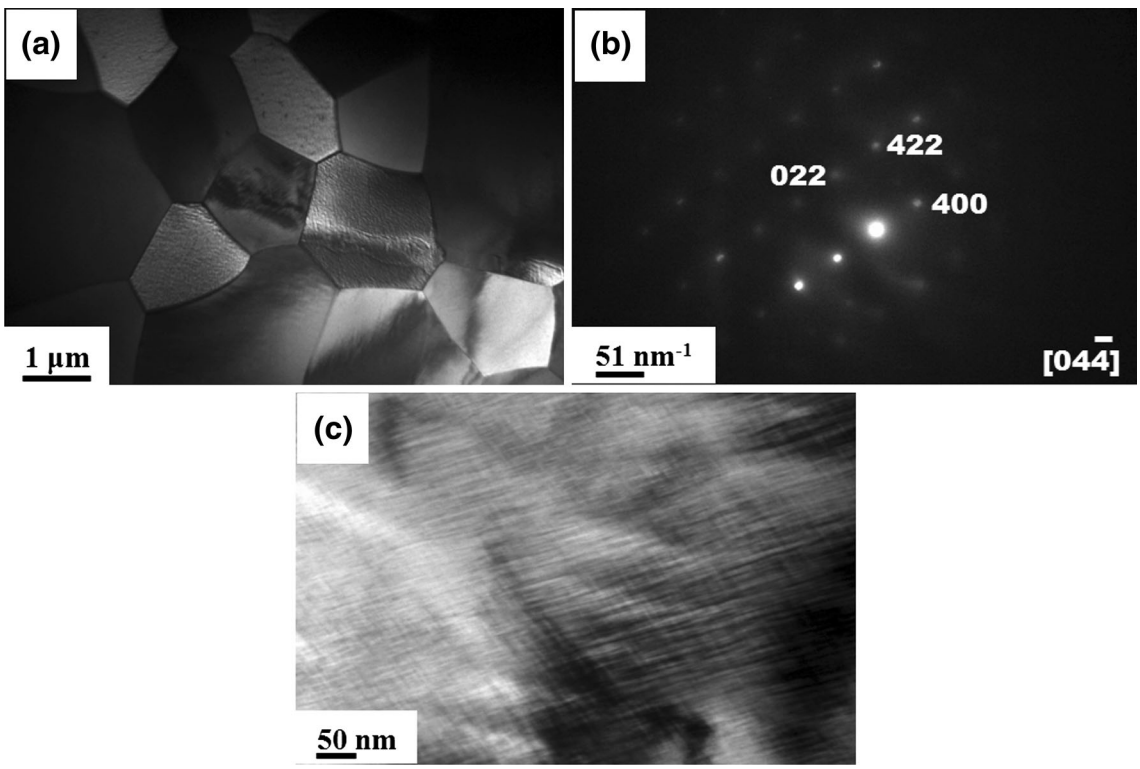

Fig. 7—Transmission electron microscopy of $Ni_{50}Mn_{20}Fe_8Ga_{25}$ alloy melt spun at high wheel speed: (*a*) bright-field image showing austenite phase, (*b*) corresponding SAED pattern taken from austenite phase has been indexed B2 atomic ordering along [044̄] zone axis, and (*c*) bright-field image showing premartensitic tweed structure at higher magnification.

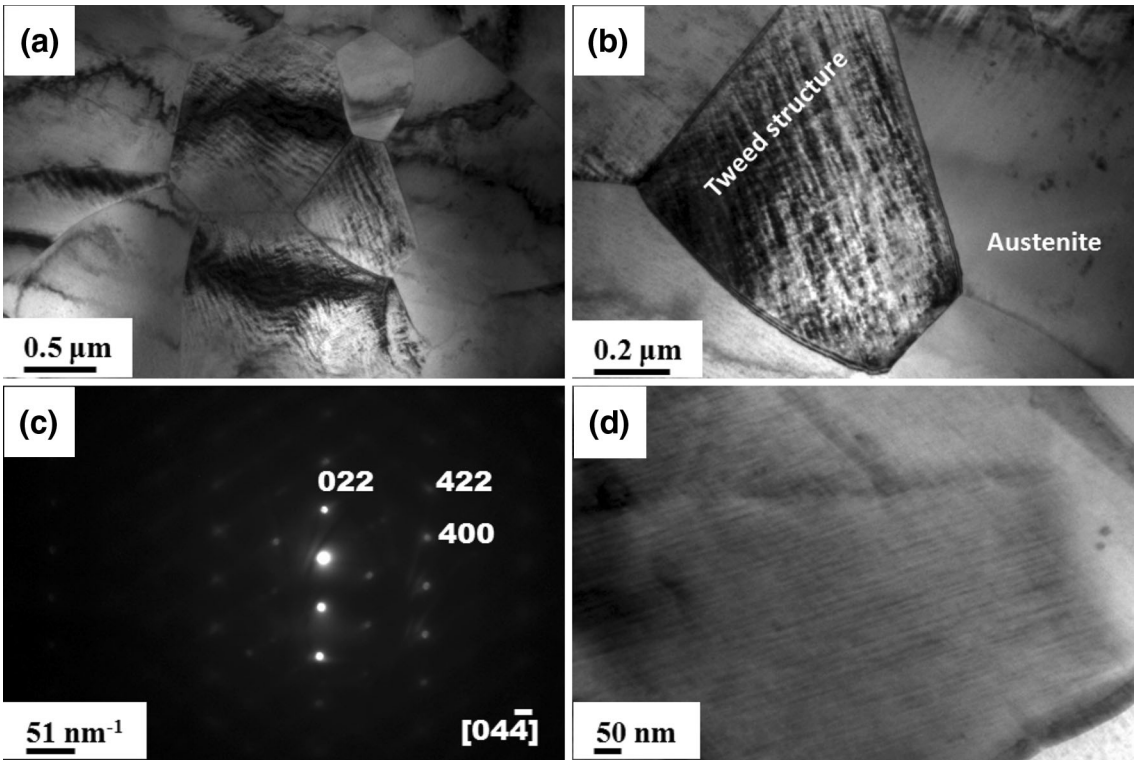

Fig. 8—Transmission electron microscopy of ribbons of $Ni_{50}Mn_{20}$ $Fe_{11}Ga_{25}$ alloy melt spun at high wheel speed of 30 m/s: (*a*) bright-field image showing mixture of austenite and premartensitic tweed structure, (*b*) similar region of phase mixture at higher magnification, (*c*) corresponding SAED pattern taken along [04$\bar{4}$] zone axis, and (*d*) bright-field image showing premartensitic tweed structure at higher magnification.

In Figure 9(c), the magnetization as a function of temperature has shown for 20 m/s wheel speed ribbons for different Fe concentrations. Martensitic transformation temperature follows a linear trend and increases in accordance with the Fe content; however, Curie temperature also follows a similar trend except for 11 at. pct Fe. Moreover, for all the conditions, magnetization decreases sharply to zero at Curie temperature. For a better understanding, martensitic transformation temperatures are also plotted as a function of average Fe content or *e*/*a* ratio for all the processing conditions as represented in Figure 10(b). Martensitic transformation temperature increases monotonously as a function of "Fe" concentration (or *e*/*a* ratio) for all the processing conditions. After annealing, the values suggest that there is a recovery in the martensitic transformation temperature. Similarly, Curie temperatures as a function of different processing conditions are plotted in Figure 10(c). It is evident that Curie temperature increases linearly as a function of "Fe" concentration (or *e*/*a* ratio) for all the processing conditions. However, there is a slight increase in the Curie temperature after annealing for 2 and 5 at. pct Fe samples and considerable increase for 8 and 11 at. pct samples.

IV. DISCUSSION

A. *Microstructure*

The formation of equiaxed fine grain size of austenite phase for the majority of the phase content of all melt-spun ribbons can be attributed to the high nucleation rate at the melt–wheel interface where the heat extraction takes place.

The 8 at. pct-Fe alloy melt spun at a low wheel speed exhibits both austenite phase as well as tweed structure. The tweed structure appears like characteristic cross-hatched pattern.[19] Earlier researchers observed tweed patterns in electron micrographs of samples at temperatures above the martensite transition temperature. Generally, these structures are observed in medium and weak martensites such as in shape memory alloys like Fe-Pd and Ni-Al. One can rationalize that the quenching of liquid during the melt-spinning process results in a higher degree of undercooling leading to higher rate of nucleation and local segregation effects during solidification. These could consequently generate local fluctuations in the concentrations and could lead to a mixture of deformed and undeformed regions as precursor tweed or premartensitic structure. Compositional inhomogeneities are often cited as reasons to the formation of premartensitic tweed structures. The trend of martensite transformation temperature (Figure 10(b)) for all these samples shows tweed-like contrast, which lies well below the room temperature, hence suggesting the precursor formation before the parent austenitic phase transforms to tetragonal martensitic phase.

In the case of 11 at. pct Fe alloy melt spun at low wheel speed, the results suggest nucleation and evolution of martensite phase from the grain boundary triple junctions. TEM bright-field images and SAED patterns confirm premartensitic tweed structures too. In general,

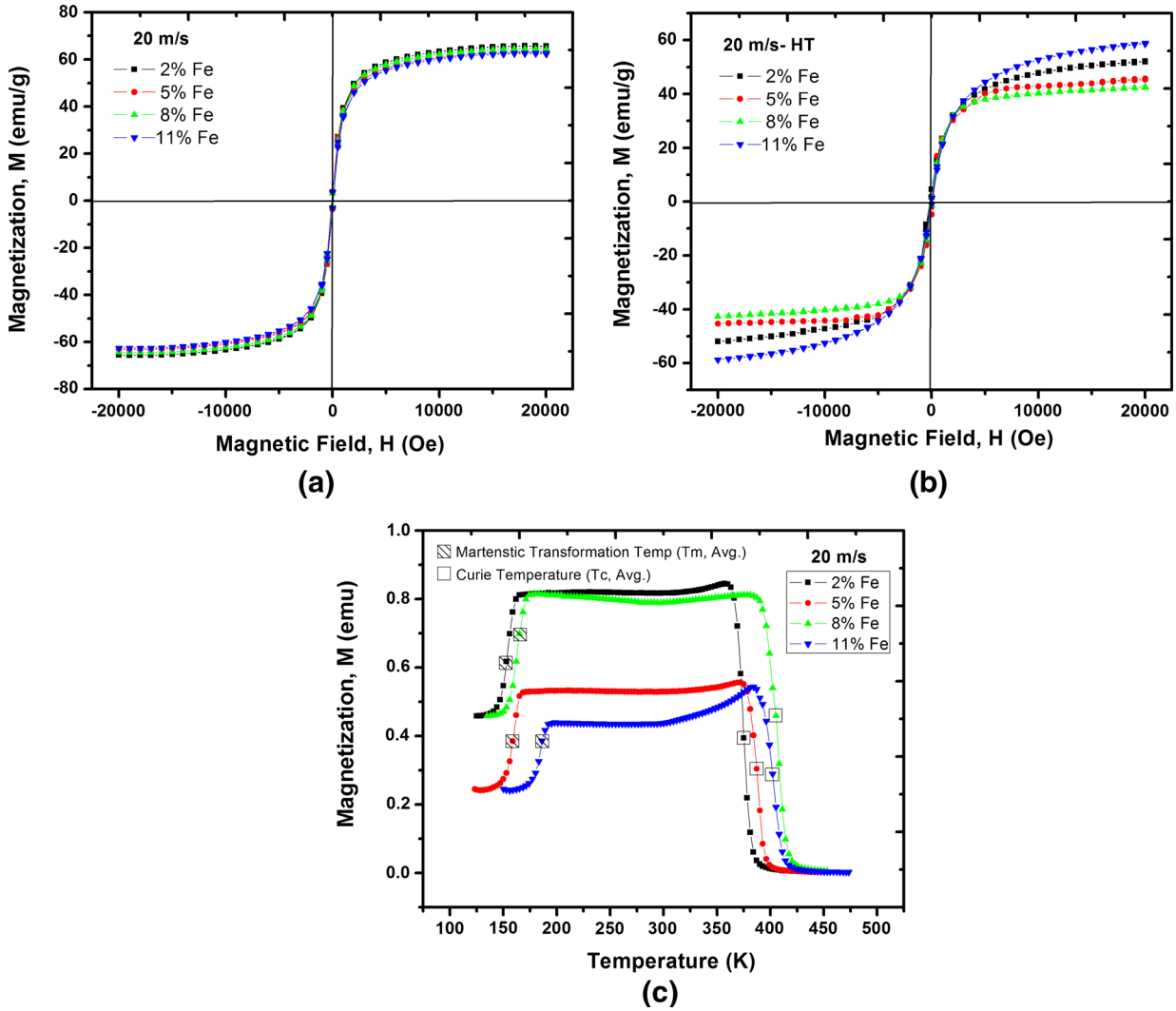

Fig. 9—(*a*) Plot of magnetization *vs* magnetic field for 20 m/s wheel speed Ni_2(Mn,Fe)Ga Heusler alloy melt-spun ribbons before and after annealing at different "Fe" concentrations. (*b*) Plot of magnetization *vs* magnetic field for 20 m/s wheel speed annealed Ni_2(Mn,Fe)Ga Heusler alloy melt-spun ribbons at different "Fe" concentrations. (*c*) Plot of magnetization *vs* temperature for 20 m/s wheel speed Ni_2(Mn,Fe)Ga Heusler alloy melt-spun ribbons at different "Fe" concentrations.

the grain boundaries are more prone to act as nucleating sites because they are the sites of high defect density. It is worth noting that (as shown in Figure 5(b)) the alternative layer of twins of martensite evolves from grain boundary triple junctions. Grain boundary triple junctions could provide a suitable site for defect density and thus attribute to nucleation of martensite.[21] These secondary phases are at a low volume fraction that cannot be detected by XRD but could play an important role in determining the final magnetic properties of the samples.

A phase analysis of 2 at. pct-Fe and 5 at. pct-Fe samples melt-spun at low wheel speed showed no premartensitic tweed structures perhaps because these samples are disordered to a lower extent than the 8 at. pct-Fe and 11 at. pct-Fe alloy samples. A higher concentration of quenched-in defects results in more disorder and can lead to the formation of tweed structures.

As noted in Section III–A, the phase evolution for samples melt spun at higher speeds is different from the samples melt spun at lower speeds. Accordingly, the magnetic properties are correlated as follows.

All the ribbons melt spun at high wheel speeds resulted in austenite phase with B2 ordering for all the "Fe" concentrations explored in this study and contained premartensitic tweed structures. As discussed earlier, the higher under cooling and higher "Fe" concentration would resulted in premartensitic tweed structures; the same argument is true for higher-speed (30 m/s) ribbons.

In addition, the annealed samples at 1273 K (1000 °C)/1 hour for all the low-speed (20 m/s) and high-speed (30 m/s) melt-spun ribbons for all "Fe" concentrations exhibits $L2_1$ Heusler atomic ordering as is clear from the XRD analysis. In general, the transformation sequence is B2 (austenite) to $L2_1$ (austenite) as explained in the order–disorder diagram

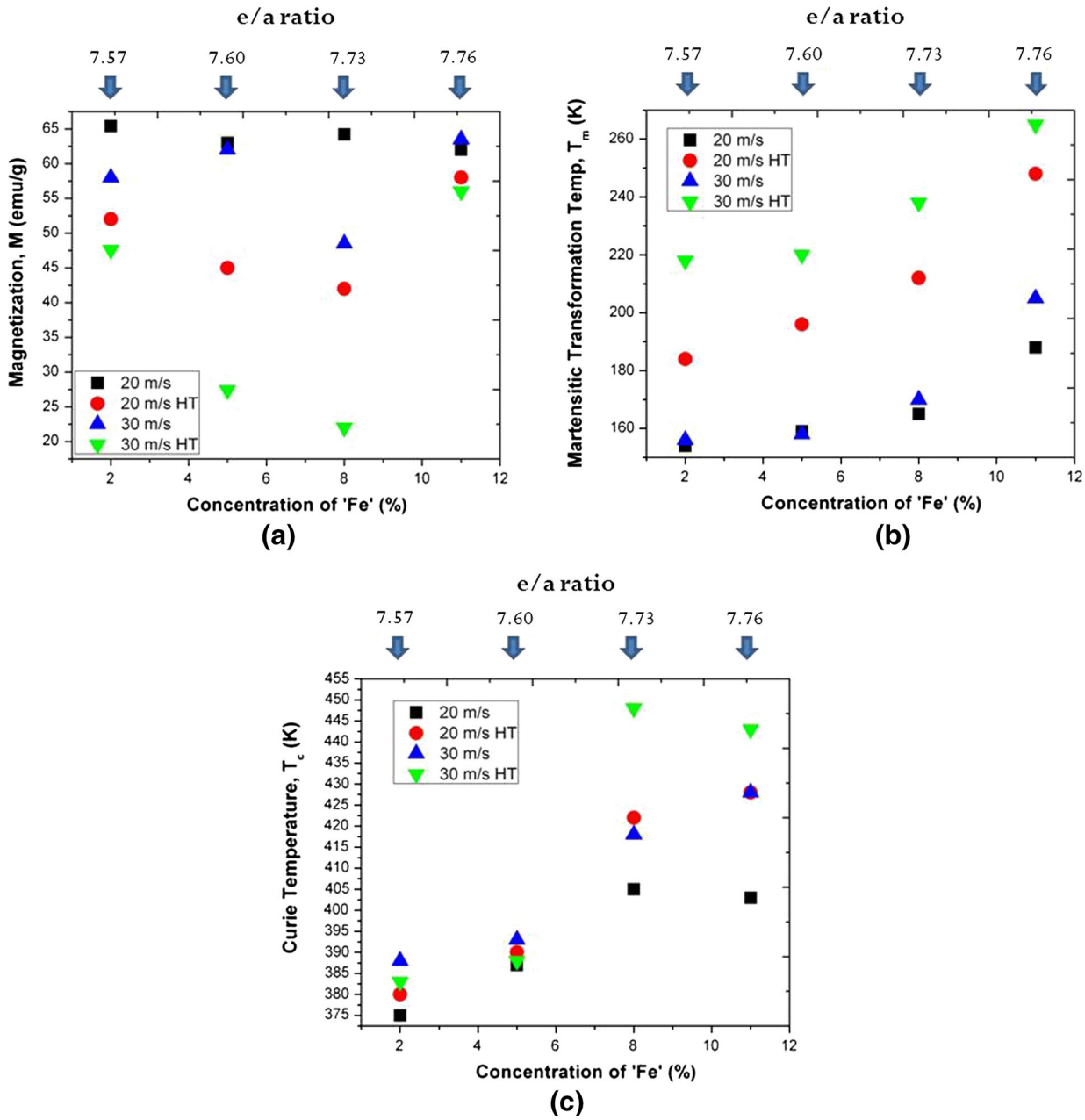

Fig. 10—(*a*) Effect of iron content on saturation magnetization, the *e*/*a* values for corresponding average compositions are given in the *x*-axis at the top. (*b*) Effect of iron content on martensite transformation temperature; the *e*/*a* values for corresponding average compositions are given in the *x*-axis at the top. (*c*) Effect of iron content on Curie temperature; the *e*/*a* values for corresponding average compositions are given in the *x*-axis at the top.

in Figure 3 of Reference 22. It is evident that these samples annealed at 1273 K (1000 °C) for 1 hour and furnace cooled have undergone slow cooling that has given sufficient time for ordering to result in $L2_1$ structure.

B. *Magnetic and Structural Properties*

As described in the results (Figures 9(a) and (b), and 10(a)), the magnetic moment is not following any particular trend; rather it fluctuates and decreases further upon annealing. In general, the Mn atoms in the Ni_2MnGa alloy will be responsible for the magnetic moment, and in this case, as Mn is replaced by Fe, the net magnetic moment should decrease. Usually, the magnetic moment is calculated from individual austenite and martensite phases. It also depends on the structural transformations that occur during heating and cooling of these alloys. Overall, we believe each condition has a different phase content as per the processing history, and a varying Fe content replaced with Mn would lead to fluctuations in the magnetic moment. However, it may not be true always, and *e*/*a* ratio would be the better parameter to describe magnetic moment as mentioned by the earlier researchers.[18,23] Corresponding results are comparable.

Martensitic transformation temperature (T_m) and Curie temperature (T_C) are very sensitive to chemical composition and e/a ratio. Martensite transformation temperature is noted to increase linearly, irrespective of processing condition, as the iron content in the alloy increases. There is a significant increase in the martensitic transformation temperature for annealed samples, and it could be attributed to a transformation from partially ordered B2 structure to $L2_1$ Heusler atomic ordered structure. Earlier researchers[20] also observed linear dependence of martensitic transformation temperature (T_m) as the e/a ratio increases from 7.57 to 7.76.

The Curie temperature shows a linear dependence with an increase in Fe concentration and is comparable with earlier literature[20] for all the processing conditions. However, Chen *et al.*[24] observed that in case of conventional solidification substitution of "Fe" from 2 to 11 at. pct would result in decreasing both martensitic transformation temperature (T_m) and Curie temperature (T_C). In our case, the processing route is rapid solidification, and thus, the solubility "Fe" could be extended in comparison to conventional solidification. Moreover, the rapid solidification resulted in the quenched short-range disorder, which in turn attributed to the decrease in Curie temperature and martensite transformation temperatures, which are recovered after annealing due to rearrangement of atoms by diffusion and due to highly ordered $L2_1$ phase.[25,26] Overall, the martensitic transformation temperature and Curie temperature show an increasing trend in accordance with Fe content in the alloy and a slight enhancement is observed for all the samples upon annealing. However, for 11 at. pct Fe doped alloy, Curie temperature decreases for 20 m/s and 30 m/s annealed ribbons. This could be due to respective phase content and processing history of the corresponding alloy.

V. CONCLUSIONS

1. A Ni_2(Mn,Fe)Ga Heusler alloy with austenite phase (B2 partial atomic ordering) resulted from both the wheel speeds for all "Fe" concentrations. Premartensitic tweed structures are observed in low wheel speed ribbon of higher "Fe" concentrations (8 and 11 at. pct) and high wheel speed ribbons of all "Fe" concentrations (2, 5, 8, and 11 at. pct).
2. Annealing at 1273 K (1000 °C) for 1 hour favors austenite phase with $L2_1$ Heusler atomic order for both the wheel speeds for alloys of all iron contents explored in this study.
3. The saturation magnetization values are sensitive to microstructure, composition inhomogeneities, and e/a ratio.
4. The martensitic transformation temperature and Curie temperature show increasing trend with increasing Fe content for all the processing conditions. Further improvement is noted in annealed samples.
5. A desirable combination of properties such as a saturation magnetization value of 56.0 emu/g, martensitic transformation temperature of 265 K (−8 °C), and Curie temperature of 443 K (170 °C) is achieved for 11 at. pct-Fe alloy ribbon melt spun at a high wheel speed and annealed at 1273 K (1000 °C) for 1 hour.

ACKNOWLEDGMENTS

The authors thank Dr. Bhaskar Majumdar, Defence Metallurgical Research Laboratory, for experimental facilities and useful discussions.

REFERENCES

1. K. Ullakko, J.K. Huang, C. Kantner, V.V. Kokorin, and R.C. O'Handley: *Appl. Phys. Lett.*, 1996, vol. 69, pp. 1966–68.
2. M.L. Richard, J. Feuchtwanger, S.M. Allen, R.C. O'Handley, P. Lazpita, J.M. Barandiaran, J. Gutierrez, B. Ouladdiaf, C. Mondelli, T. Lograsso, and D. Schlagel: *Phil. Mag.*, 2007, vol. 87, pp. 3437–47.
3. D. Niklasch, J. Dadda, H.J. Maier, and I. Karman: *J. Mater. Sci.*, 2008, vol. 43, pp. 6890–901.
4. M.E. Gruner, P. Entel, I. Opahle, and M. Richter: *J. Mater. Sci.*, 2008, vol. 43, pp. 3825–31.
5. J.Y. Liu, H. Lu, J.M. Chen, C. Alain, and T. Wu: *J. Mater. Sci.*, 2008, vol. 43, pp. 4921–28.
6. H.B. Wang, F. Chen, Z.Y. Gao, W. Cai, and L.C. Zhao: *Mater. Sci. Eng. A*, 2006, vols. 438–440, pp. 990–93.
7. D. Soto, F.A. Hernández, T. Krenke, H. Flores-Zúñiga, X. Moya, L. Mañosa, A. Planes, S. Aksoy, and M. Acet: *Phys. Rev. B*, 2008, vol. 77, p. 184103.
8. O. Söderberg, K. Koho, T. Sammi, X.W. Liu, A. Sozinov, N. Lanska, and V.K. Lindroos: *Mater. Sci. Eng. A*, 2004, vol. 378, pp. 389–93.
9. O. Heczko, P. Svec, D. Janickovic, and K. Ullakko: *IEEE Trans. Magn.*, 2002, vol. 38, pp. 2841–43.
10. R.V.S. Prasad and G. Phanikumar: *J. Mater. Sci.*, 2009, vol. 44, pp. 2553–59.
11. R.V.S. Prasad and G. Phanikumar: *Mater. Sci. Forum*, 2010, vol. 649, pp. 35–40.
12. D. Akahoshi, R. Hatakeyama, M. Nagao, T. Asaka, Y. Matsui, and H. Kuwahara: *Phys. Rev. B*, 2008, vol. 77, p. 054404.
13. I.M. Robertson and C.M. Wayman: *Metallography*, 1984, vol. 17, pp. 149–63.
14. S. Shapiro, J.Z. Larese, Y. Noda, S.C. Moss, and L.E. Tanner: *Phys. Rev. Lett.*, 1986, vol. 57, pp. 3199–3202.
15. S. Bysakh, P.K. Das, and K. Chattopadhyay: *Mater. Sci. Eng. A*, 2001, vols. 304–306, pp. 608–11.
16. V.A. Chernenko, J. Pons, C. Seguí, and E. Cesari: *Acta Mater.*, 2002, vol. 50, pp. 53–60.
17. A.G. Khachaturyan, S.M. Shapiro, and S. Semenovskaya: *Phys. Rev. B*, 1991, vol. 43, pp. 10832–43.
18. S. Kartha, J.A. Krumhansl, J.P. Sethna, and L.K. Wickham: *Phys. Rev. B*, 1995, vol. 52, pp. 803–21.
19. S. Kartha, T. Castan, J.A. Krumhansl, and J.P. Sethna: *Phys. Rev. Lett.*, 1991, vol. 67, pp. 3630–33.
20. X. Jin, M. Marioni, D. Bono, S.M. Allen, R.C. O'Handley, and T.Y. Hsu: *J. Appl. Phys.*, 2002, vol. 91, pp. 8222–24.
21. K. Tsuzaki, N. Harada, and T. Maki: *J. Phys. IV*, 1995, vol. 5, pp. C8–167.
22. R.W. Overholser, M. Wuttig, and D.D. Neumann: *Scripta Mater.*, 1999, vol. 40, pp. 1095–1102.
23. K. Tsuchiya, A. Ohashi, D. Ohtoyo, H. Nakayama, M. Umemoto, and P.G. McCormick: *Mater. Trans., JIM*, 2000, vol. 8, pp. 938–42.
24. F. Chen, H.B. Wang, Y.F. Zheng, W. Cai, and L.C. Zhao: *J. Mater. Sci.*, 2005, vol. 40, pp. 219–21.
25. J. Pons, C. Seguí, V.A. Chernenko, E. Cesari, P. Ochin, and R. Portier: *Mater. Sci. Eng. A*, 1999, vols. 273–275, pp. 315–19.
26. V.A. Chernenko, E. Cesari, J. Pons, and C. Seguí: *J. Mater. Res.*, 2000, vol. 15, pp. 1496–1504.